Bistability and chaos in the Taylor-Green dynamo

Rakesh K. Yadav,[1,*] Mahendra K. Verma,[1] and Pankaj Wahi[2]
[1]*Department of Physics, Indian Institute of Technology, Kanpur 208016, India*
[2]*Department of Mechanical Engineering, Indian Institute of Technology, Kanpur 208016, India*
(Received 22 September 2011; revised manuscript received 18 November 2011; published 6 March 2012)

Using direct numerical simulations, we study dynamo action under Taylor-Green forcing for a magnetic Prandtl number of 0.5. We observe bistability with weak- and strong-magnetic-field branches. Both the dynamo branches undergo subcritical dynamo transition. We also observe a host of dynamo states including constant, periodic, quasiperiodic, and chaotic magnetic fields. One of the chaotic states originates through a quasiperiodic route with phase locking, while the other chaotic attractor appears to follow the Newhouse-Ruelle-Takens route to chaos. We also observe intermittent transitions between quasiperiodic and chaotic states for a given Taylor-Green forcing.

DOI: 10.1103/PhysRevE.85.036301 PACS number(s): 47.20.Ky, 91.25.Cw, 52.65.Kj, 47.65.−d

I. INTRODUCTION

Dynamo theory has been applied to explain generation and properties of magnetic fields present in celestial bodies [1–3]. In this mechanism, a small magnetic field fluctuation is amplified by the currents induced by the motion of the conducting fluid. The growth of the magnetic field could be either due to a linear instability or a nonlinear instability. The kinematic dynamo, which involves a small magnetic field for a given velocity configuration, is an example of a linearly unstable dynamo in which the magnetic field grows or decays exponentially. Nonlinear dynamos incorporate the complete set of nonlinear interactions of the magnetohydrodynamic (MHD) equations. The transition from fluid to dynamo state in the initial phases is called a "dynamo transition." An important investigation in dynamo research is whether the dynamo transition is supercritical or subcritical. In supercritical bifurcation, the magnetic field perturbation grows monotonically as μ exceeds μ_c, where μ is a system parameter and μ_c is a critical value of the parameter for the transition. Also, the amplitude of the steady-state magnetic field grows as $\sqrt{\mu - \mu_c}$, whereas, in subcritical bifurcation, the corresponding magnetic field magnitude exhibits a sudden jump, as well as hysteresis, near the transition.

As a result of the nonlinearity, the nature of the transition is very rich, exhibiting a host of interesting behavior, including supercritical or subcritical bifurcations [4–8], a variety of dynamo states [7,9], multiple coexisiting attractors [7], etc. The magnetic field of the Earth is temporally and spatially chaotic [10]. The solar magnetic field is spatially random, but the sun-spot cycle appears to indicate that the primary dipolar field is quasiperiodic [11]. In the von Kármán sodium (VKS) experiment, Monchaux *et al*. [9] and Pétrélis *et al*. [12] reported various dynamo states, including constant, periodic, quasiperiodic, and chaotic magnetic fields. In this paper, we will study dynamo transition in the Taylor-Green dynamo. Our analysis is based on the total energy as well as the large-scale modes.

It has been found that the nature of dynamo onset depends critically on various system properties, e.g., the magnetic Prandtl number (ratio of the kinematic viscosity and the magnetic diffusivity), forcing function, system geometry, rotation frequency, etc. Note that the magnetic Prandtl number (Pm) of liquid metals and the convective fluids of the Earth's outer core and the Sun is very small (of the order of 10^{-5}), while that of the intergalactic medium is very large (around 10^{14}). In this paper, we explore the nature of dynamo for a magnetic Prandtl number of 0.5.

A strong motivation for dynamo research is to understand the nature of geodynamo and solar dynamo. To this end, scientists attempt to study the possible dynamo states and the extent of the induced magnetic field in these systems. The magnetic Reynolds number Rm (ratio of magnetic advection and magnetic diffusion) of the geodynamo is estimated to be around 125 [10], which is somewhat near the dynamo transition, so we expect our present work on dynamo transition to be relevant for the geodynamo. For the geodynamo, the ratio of the magnetic energy and the kinetic energy is large [10]. Hence, it is called a strong-field dynamo. Roberts [13] argued that a rotating sphere with magnetoconvection could show bistability with a weak- and a strong-field branch. Pierre [14] and Stellmach and Hansen [15] reported the occurrence of such dynamo branches in rotating convection in Cartesian geometry. Kuang and Bloxham [16] numerically simulated the convective dynamo in a rotating spherical shell and observed a weak-field dynamo solution in a simplified system, and strong-field dynamo solutions in a more realistic system. In this paper, we will show that similar bistability is exhibited in the box geometry without rotation or convection.

Morin and Dormy [6] performed numerical simulation in a rotating spherical shell with thermally driven convection and showed that the dynamo transition shifts from supercritical to subcritical as the magnetic Prandtl number is decreased. Krstulovic *et al*. [17] observed similar behavior in a low-dimensional model. Numerical simulations of the Taylor-Green (TG) dynamo by Ponty *et al*. [4] demonstrate that low-Pm TG dynamo shows subcriticality, while with Pm = 1 (and higher values, probably) the TG dynamo shows supercriticality, a result also observed by Yadav *et al*. [7]. We will revisit the issue of subcriticality in this paper.

Ponty *et al*. [18] have reported that the Rm required to sustain a dynamo tends to increase rapidly for lower magnetic

*yadav.r.k.87@gmail.com

Prandtl numbers. This makes direct numerical simulation of flows with small Pm progressively difficult. For example, the Rm for the dynamo transition in the VKS experiment is around 20. Since liquid sodium has Pm $\approx 10^{-5}$, the critical Reynolds number touches Rm/Pm $= 20/10^{-5} \approx 10^6$ [9], which is beyond the computational power of the present-day supercomputers due to the requirement of very high numerical grid resolution. However, many researchers have modeled such extreme parameters using hyperdissipation, large-eddy simulations [18], and shell models [5,8]. We use Pm $= 0.5$, which allows us to investigate the TG dynamo in reasonable detail using relatively coarse grid resolution.

Earlier, Nore *et al.* [19] simulated the TG dynamo for Pm near unity. Ponty *et al.* [4] observed a subcritical dynamo bifurcation for the TG dynamo in the low-Pm regime. Mininni *et al.* [20] and Yadav *et al.* [7] studied the energy transfers and the geometry of the velocity and the magnetic field structures. Yadav *et al.* [7] also observed a supercritical pitchfork bifurcation for the dynamo transition at Pm $= 1$. Dubrulle *et al.* [21] investigated various bifurcations in both hydrodynamic (with no magnetic field) and magnetohydrodynamic systems under TG forcing. Scientists have also studied dynamo behavior for various kinds of forcing, e.g., Roberts, ABC, Ponomarenko, and random, as well as for different geometries, e.g., box, cylinder, sphere, etc. [22]. Dynamo transition and subsequent dynamo states have also been studied using low-dimensional models of the dynamo [23].

The outline of the paper is as follows: The numerical procedure is described briefly in Sec. II. Bifurcation analysis is presented in Sec. III. We analyze several chaotic states and the routes to chaos in Sec. IV. We conclude in Sec. V.

II. SIMULATION METHODOLOGY

The governing equations of the dynamo for an incompressible fluid with unit density are

$$\partial_t \mathbf{u} + (\mathbf{u}\cdot\nabla)\mathbf{u} = -\nabla p + (\mathbf{J}\times\mathbf{B}) + \nu\nabla^2\mathbf{u} + \mathbf{F}, \quad (1)$$

$$\partial_t \mathbf{B} = \nabla\times(\mathbf{u}\times\mathbf{B}) + \eta\nabla^2\mathbf{B}, \quad (2)$$

$$\nabla\cdot\mathbf{u} = 0, \quad (3)$$

$$\nabla\cdot\mathbf{B} = 0, \quad (4)$$

where $\mathbf{u}$ is the fluid velocity, $\mathbf{B}$ is the magnetic field, $\mathbf{J} = \nabla\times\mathbf{B}$ is the current density, p is the hydrodynamic pressure, ν is the kinematic viscosity, η is the magnetic diffusivity, and $\mathbf{F}$ is the external force field. The three important parameters related to dynamo instability are the magnetic Prandtl number Pm $= \nu/\eta$, the Reynolds number Re $= UL/\nu$, and the magnetic Reynolds number Rm $= UL/\eta$, where U and L are the large velocity scale and the large length scale, respectively. Note that Rm $=$ Re $\times$ Pm, hence only two of the above three parameters are independent. In our study, we fix the magnetic Prandtl number to 0.5 with $\nu = 0.1$ and $\eta = 0.2$.

We solve the MHD equations (1)–(4) numerically in a box geometry of size $(2\pi)^3$ with periodic boundary conditions in all the directions. We use a pseudospectral code TARANG [24] to carry out our simulations. We apply the fourth-order Runge-Kutta scheme for time advancement with dynamically adjusted $dt = \Delta x/\sqrt{20E^u}$ [the Courant-Friedrichs-Lewy (CFL) condition], where Δx is the grid spacing and E^u is the total kinetic energy. On the velocity field, we apply the Taylor-Green forcing

$$\mathbf{F}(k_0) = F_0 \begin{bmatrix} \sin(k_0x)\cos(k_0y)\cos(k_0z) \\ -\cos(k_0x)\sin(k_0y)\cos(k_0z) \\ 0 \end{bmatrix}, \quad (5)$$

where F_0 is the amplitude of the forcing and k_0 is the wave number. We set k_0 equal to 2. Note that the TG force field has components only along the x and y directions. Numerical simulations reveal that the TG forcing induces counter-rotating eddies, and it has certain qualitative similarities with the VKS experiment [9] and the spherical-shell dynamo with rotation (to be discussed later).

The simulation box is uniformly discretized in all the directions using 64^3 grid points. This resolution was sufficient to resolve our simulation near the dynamo transition, as demonstrated by the fact that the product of the Kolmogorov length and the largest wave number lies between 1.3 and 9 for all our runs. We also verified the grid independence by running some simulations on a 64^3 grid as well as on a 128^3 grid. All our simulations were dealiased using the 2/3 rule. We performed approximately 150 simulations for various forcing parameters with $F_0 = 1 : 46$, and studied the global kinetic and magnetic energies as well as the amplitudes of the velocity and magnetic Fourier modes. In our simulations, the magnetic Reynolds number for the dynamo states ranged from approximately 3 to 90.

The importance of large-scale modes has been amply highlighted in dynamo literature. In our present dynamo simulations, as well as for Pm $= 1$ reported earlier by Yadav *et al.* [7], some of the magnetic and kinetic Fourier modes play dominant roles. For the magnetic Reynolds numbers employed in these simulations, the dominant velocity modes are $(\pm2,\pm2,\pm2)$, $(\pm4,\pm4,\pm4)$, $(\pm4,\pm4,0)$, and the dominant magnetic modes are $(0,0,\pm1)$, $(0,0,\pm2)$, $(0,0,\pm3)$, $(\pm2,\pm2,\mp3)$, $(\mp2,\mp2,\pm1)$. Here, the three arguments refer to the x, y, and z components of the wave number in the Fourier space. The $(\pm2,\pm2,\pm2)$ velocity modes contain maximum kinetic energy due to the TG forcing at $k_0 = 2$. The above set of modes carries more than 95% of the total energy. Note, however, that higher wave number velocity and magnetic Fourier modes become important in turbulent dynamos. We also point out that the above modes play similar roles as the large-scale modes described in the earlier dynamo studies [1,25].

In this paper, we analyze time series and phase-space plots of the Fourier modes. This exercise provides us with information about various dynamo states as well as the nature of bifurcations. Primary and secondary instabilities can be conveniently illustrated using bifurcation diagrams. In the next section, we will describe bifurcation diagrams constructed using globally averaged quantities and some of the dominant magnetic Fourier modes.

III. BIFURCATION ANALYSIS AND WEAK AND STRONG DYNAMO BRANCHES

To understand various dynamo states of the TG dynamo, as well as their origin, we construct a bifurcation diagram by plotting the ratio of the total magnetic energy and the

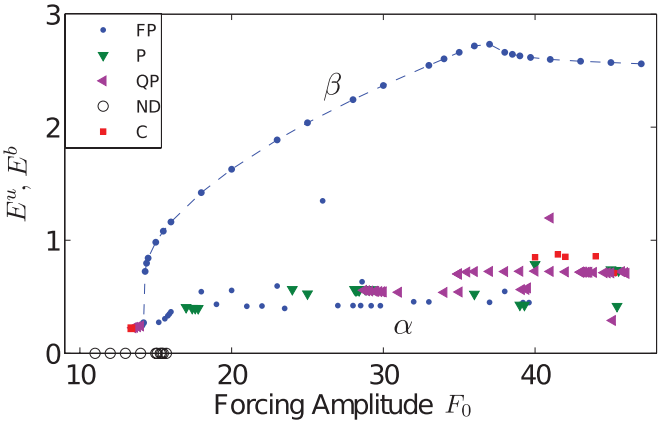

FIG. 1. (Color online) Bifurcation diagram: Ratio of the total magnetic energy and the total kinetic energy (E^b/E^u) vs the forcing amplitude F_0. In the figure, ND = no-dynamo state, FP = fixed point (constant in time), P = periodic state, QP = quasiperiodic state, and C = chaotic state.

total kinetic energy (E^b/E^u) as a function of the TG forcing parameter F_0. These quantities are computed for the steady states. An average value is taken for periodic and chaotic dynamo states. In Fig. 1, we plot the time-averaged values of E^b/E^u versus F_0, which demonstrates the presence of various dynamo states including no-dynamo, fixed point (constant in time), periodic, quasiperiodic, and chaotic configurations. The figure shows two distinct features: (1) a finite jump in the magnetic field during the transition; (2) two distinct classes of dynamo states labeled by "α" and "β." An important point to note is that multiple states could exist for a given F_0. Hence, to keep ourselves on a particular branch, we use the final state of a dynamo state with a smaller F_0 as an initial condition for the dynamo with a larger F_0.

Similar features are observed in Fig. 2 in which we plot E^b versus Rm. The two branches α and β are quite distinctive. The magnetic energy E^b, as well as the ratio E^b/E^u, are larger for the β branch than that for the α branch. Thus, we call the former a "strong-field" branch and the latter a "weak-field" branch. The scatter in the data points in the figure is due to the numerous secondary bifurcations. A jump in E^b, as well

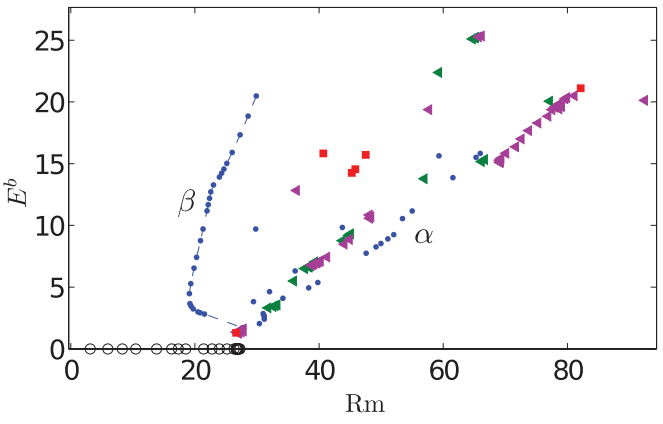

FIG. 2. (Color online) Bifurcation diagram: Total magnetic energy (E^b) vs the magnetic Reynolds number (Rm). Description of different symbols is provided in Fig. 1.

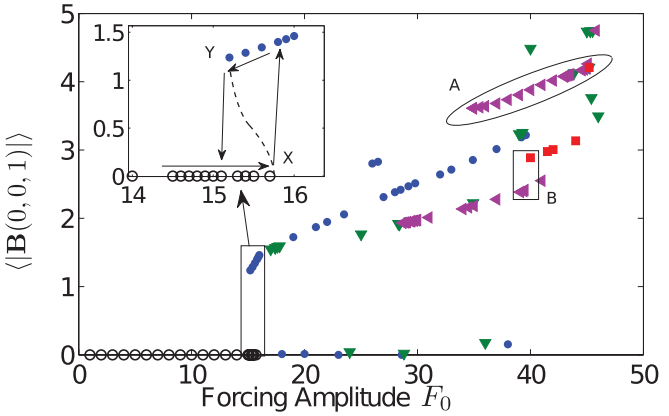

FIG. 3. (Color online) Bifurcation diagram: Time-averaged values of $|\mathbf{B}(0,0,1)|$ for various forcing amplitude F_0. The inset for $F_0 =$ 14:16 illustrates a sudden jump and a hysteresis loop indicating that the transition is subcritical. Also, oval A exhibits the quasiperiodic route to chaos (see Sec. IV A), and the rectangular box B exhibits the Newhouse-Ruelle-Takens route to chaos (see Sec. IV B). Description of different symbols is provided in Fig. 1.

as the kneelike feature in the β branch, demonstrate that the dynamo transition is subcritical. The origin of subcriticality and "bistability" (dual branches) is intriguing, which will be explored using large-scale Fourier modes.

As described in Sec. II, the dominant magnetic modes are $\mathbf{B}(0,0,1)$ and $\mathbf{B}(0,0,2)$. We redo the bifurcation analysis using the magnetic Fourier modes $\mathbf{B}(0,0,1)$ and $\mathbf{B}(0,0,2)$ as the relevant quantities. It is noteworthy that the mode $\mathbf{B}(0,0,1)$ is the most dominant one in the α branch. On the contrary, $\mathbf{B}(0,0,2)$ is the dominant mode in the β branch with $\mathbf{B}(0,0,1) \approx 0$. We also observe that for an arbitrary initial condition, the α branch is much more likely than the β branch. That is, the basin of attraction for the α branch is much larger compared to the β branch. Moreover, the α branch shows richer bifurcations than the β branch in the parameter regime studied in this paper. In Fig. 3, we plot the time-averaged values of the magnitude of $\mathbf{B}(0,0,1)$ for various F_0 in the α branch. We do not plot the β branch dynamo states in this figure to avoid cluttering. Since the Fourier amplitudes are generally complex, it is convenient to use the absolute value of a Fourier mode to depict the dynamo states. Note that for some of the dynamo states, $\langle|\mathbf{B}(0,0,1)|\rangle$ is negligible, as shown by the data points near the F_0 axis of Fig. 3. For these states, other modes in the α branch, which mostly carry small energy, become dominant, for instance, the $\mathbf{B}(0,0,3)$ mode.

The jump in the value of $\langle|\mathbf{B}(0,0,1)|\rangle$ provides further insights into subcriticality. The inset of Fig. 3 shows an enlarged view of the dynamo transition region near $F_0 = 15.8$. We first observe a dynamo state at approximately $F_0 = 15.8$, for which $|\mathbf{B}(0,0,1)|$, as well as the E^b, shows a finite jump. However, when we use the dynamo state at $F_0 = 15.8$ as our initial condition and gradually decrease the forcing amplitude, as shown in the inset of Fig. 3, the dynamo state continues until $F_0 \approx 15.2$, at which point there is a sudden jump to the fluid state. This feature of hysteresis for $F_0 =$ 15.2:15.8 demonstrates the subcritical nature of the dynamo transition, with a "subcritical pitchfork bifurcation" at X and a "saddle-node bifurcation" at Y (see the inset of Fig. 3). These

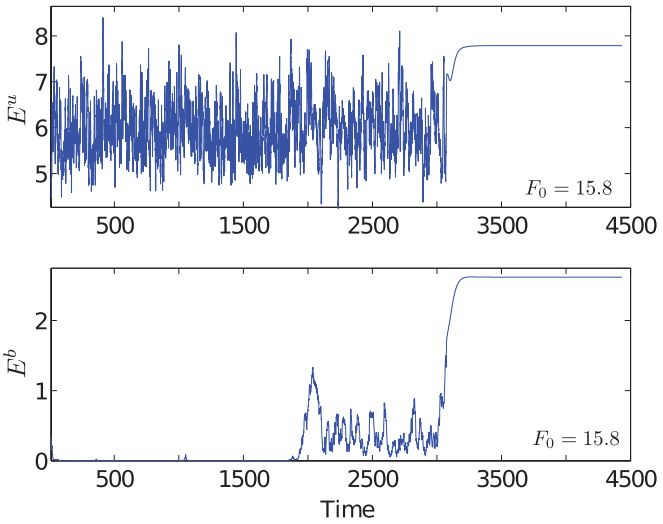

FIG. 4. (Color online) The total kinetic energy (top panel) and the total magnetic energy (bottom panel) for a forcing amplitude of 15.8, indicating a constant value for the field in the steady state.

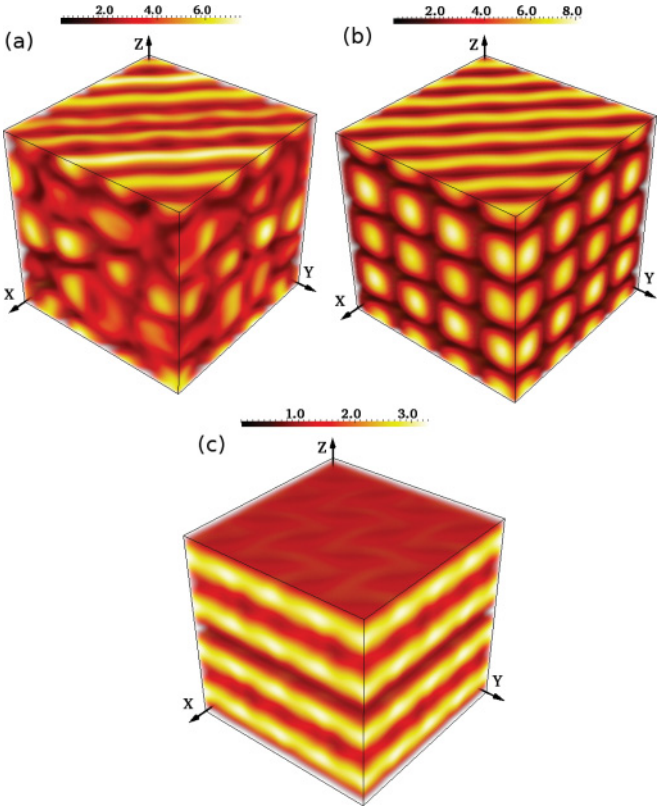

FIG. 5. (Color online) Three-dimensional volume rendering of velocity and magnetic field for $F_0 = 15.2$ near the dynamo transition. (a) Spatially chaotic velocity field for no-dynamo state. (b) Uniform velocity field for the dynamo state due to the suppression of chaos in the presence of finite mean magnetic field. (c) Uniform magnetic field structure for the dynamo state. Note that magnetic field of (c) does not contain $\mathbf{B}(0,0,2)$. It is, in fact, an approximate superposition of $\mathbf{B}(0,0,1)$, $\mathbf{B}(0,0,3)$, and $\mathbf{B}(0,0,5)$ modes.

points are joined together using a dashed curve to depict the unstable branch. In a recent study, Krstulovic *et al*. [17] also observed a subcritical dynamo transition in their simulation and low-dimensional model. Morin and Dormy [6] observed a subcritical dynamo transition for lower magnetic Prandtl numbers in the spherical-shell dynamo. Using shell models, Sahoo *et al*. [8] have reported a subcritical dynamo transition for Pm as low as 10^{-4}. In a planetary dynamo context, Kuang *et al*. [26] argued that the sudden termination of the Martian dynamo could be due to the subcriticality.

Another noteworthy feature during the dynamo transition is that the Re is sufficiently high ($\approx$60) for the fluid to be temporally chaotic in the no-dynamo state. However, at the same F_0, both the temporal and spatial fluctuations in velocity field are suppressed in the corresponding dynamo state. Figure 4 contains the time evolution of a dynamo state at $F_0 = 15.8$, while Fig. 5 exhibits the volume-rendered velocity and magnetic fields for a no-dynamo state and a dynamo state near the dynamo transition. The suppression of chaotic modulations in the velocity field after the dynamo transition is due to the presence of the newly born finite magnetic field. Morin and Dormy [6] reported similar effects of magnetic field in their simulations. After $F_0 \approx 16.2$, the dynamo solution bifurcates to periodic states, and subsequently to quasiperiodic and chaotic states as shown in Fig. 3.

The dynamo transition of the β branch differs significantly from that of the α branch described earlier. We highlight the differences in Fig. 6. For the α branch, the jumps in the kinetic and magnetic energies shown in Fig. 6(a) are consistent with the subcritical nature of the transition described earlier. However, the β branch exhibits chaos at the dynamo transition itself. The origin of the chaotic state becomes apparent when we decrease F_0 from the fixed point solution. As shown in Fig. 6(b), the fixed point bifurcates to quasiperiodic (triangular data points) and, subsequently, to chaotic state (square data point) as the F_0 is decreased. The route to chaos for the β branch may be similar to that observed by Pal *et al*. [27] for zero Prandtl number convection. The quasiperiodic and the chaotic states are clustered in Fig. 1 near the transition.

The weak- and the strong-field branches of the dynamo have been reported in the context of convection-driven hydromagnetic dynamos [13,16,29,30]. Pierre [14] and Stellmach and Hansen [15] numerically demonstrated this phenomenon in the Childress-Soward dynamo where they reported that the strong-field branch goes even further back than the weak-field branch in the parameter space, analogous to the β branch reported in this paper. Similar behavior has also been reported by Sreenivasan and Jones [31] in a rapidly rotating spherical dynamo. It is interesting that our system in the box geometry, without any convection or rotation, exhibits weak and strong dynamo branches.

Another significant feature of our dynamo simulation is the subcritical transition for Pm = 0.5. Note that the earlier results on convective dynamo (with rotation) by Morin and Dormy [6], and the low-dimensional model of Krstulovic *et al*. [17], indicate that the dynamo transition could shift from supercritical to subcritical as we decrease the Pm. Our subcritical dynamo transition for Pm = 0.5 supplemented by Yadav *et al*.'s [7] supercritical dynamo transition for Pm = 1 are consistent with the aforementioned works.

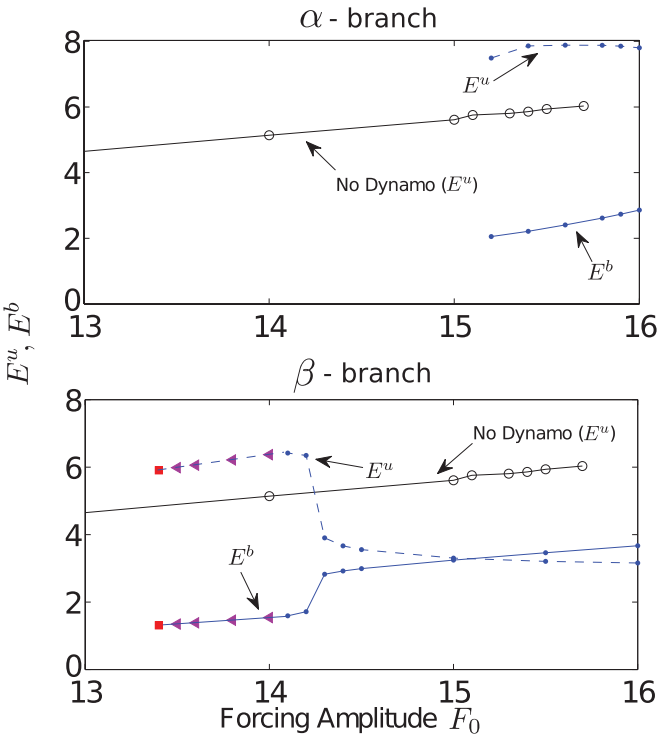

FIG. 6. (Color online) Plots of the total kinetic energy (E^u) and the total magnetic energy (E^b) vs the F_0 near the dynamo transition: (a) The α branch portrays the subcritical nature of the transition, and (b) the β branch illustrates transition from a fixed point state (filled circular data points) to a quasiperiodic state (triangular data points) and subsequently to a chaotic state (square data point) as F_0 is decreased.

The above results demonstrate common features of weak and strong dynamo branches, as well as transition from supercriticality to subcriticality with decreasing Pm, for the TG dynamo and the spherical-shell dynamo. These similarities could be due to some geometrical resemblance between the two systems. Rotating convection generates Taylor columns, with the adjacent columns having the opposite sense of rotation and helicity (see Fig. 5 in Ref. [28]). In Fig. 7, we plot the kinetic helicity $\mathbf{u} \cdot (\nabla \times \mathbf{u})$ for a dynamo state near transition. The alternating signs in the helicity are qualitatively similar to the Taylor columns in spherical dynamo simulations. This resemblance encourages us to investigate these features further. In the next section, we will focus on several chaotic dynamo states and study routes to chaos for these states.

IV. ROUTES TO CHAOS

The phase-space portraits drawn using the Fourier modes reveal multiple windows of chaos near the dynamo transition itself. In this section, we describe routes to chaos for two chaotic windows: the oval enclosure A and the rectangular box B shown in Fig. 3. In the following discussion, we show that the origin of chaos for the dynamo states of oval A follow a quasiperiodic route to chaos through phase locking, while the corresponding route to chaos for the box B is through the Newhouse-Ruelle-Takens scenario.

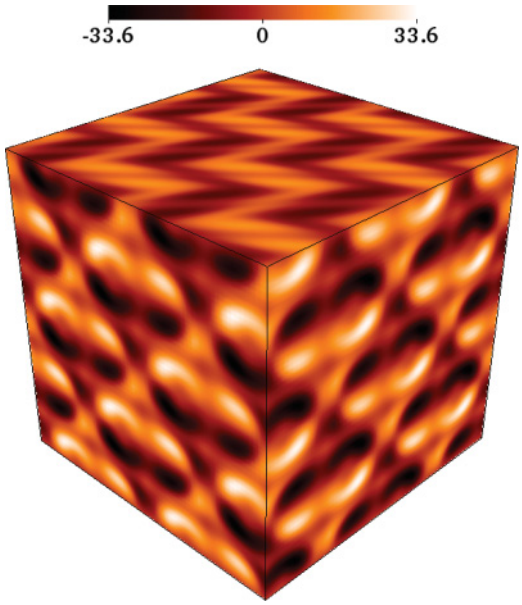

FIG. 7. (Color online) Kinetic helicity $\mathbf{u} \cdot (\nabla \times \mathbf{u})$ for the $F_0 = 15.2$ dynamo state. The alternating sign of the helicity is qualitatively similar to the Taylor columns of spherical-shell dynamo with rotation [28].

We study the routes to chaos using some of the dominant modes of the magnetic field, viz., $\mathbf{B}(0,0,1)$, $\mathbf{B}(0,0,2)$, and $\mathbf{B}(0,0,3)$. We use time series, phase-space projections, and Poincaré sections for this study [32].

A. Quasiperiodic route to chaos through phase locking

In Fig. 8, we illustrate the phase-space projections of dynamo states on the $|\mathbf{B}(0,0,1)|$-$|\mathbf{B}(0,0,3)|$ plane for the forcing range of $F_0 = 41{:}46$ (corresponding to the oval A of Fig. 3). For $F_0 = 41$, 42, and 43, the system is quasiperiodic since the phase-space projection is densely filled up. The

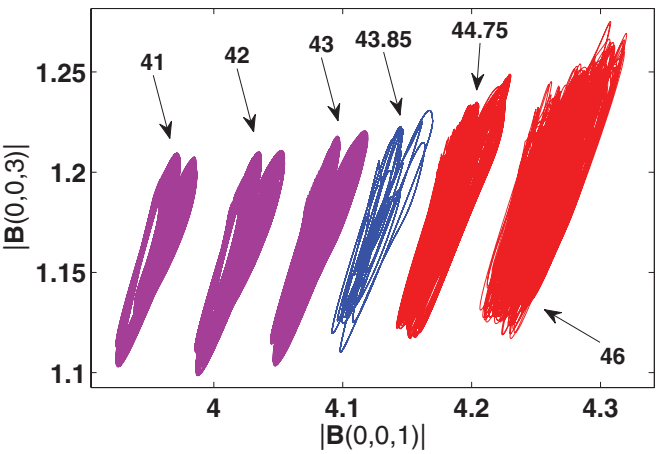

FIG. 8. (Color online) Phase-space projections on the $|\mathbf{B}(0,0,1)|$-$|\mathbf{B}(0,0,3)|$ plane demonstrating a quasiperiodic route to chaos through phase locking. The forcing amplitudes F_0 for different attractors are marked with arrows. $F_0 = 41$, 42, 43, $F_0 = 43.85$, and $F_0 = 44.75$, 46 correspond to quasiperiodic, phase-locked, and chaotic states, respectively.

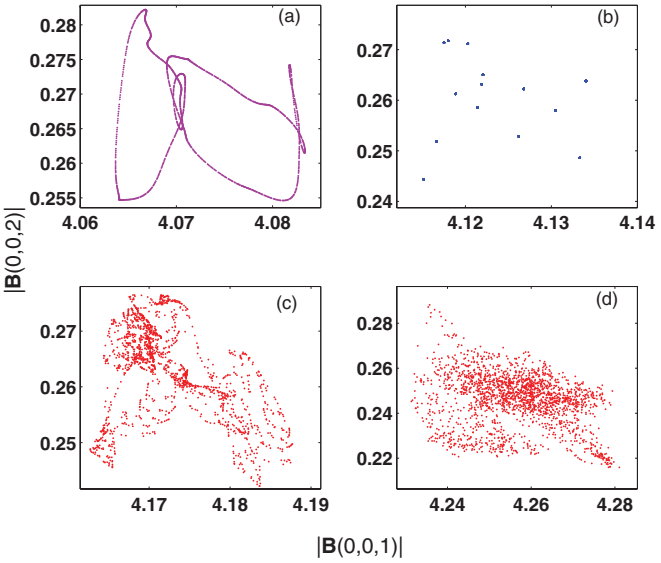

FIG. 9. (Color online) Poincaré sections of some of the attractors of Fig. 8 with $|\mathbf{B}(0,0,3)| = 1.15$ as the Poincaré plane: (a) quasiperiodic attractor for $F_0 = 43$; (b) phase-locked attractor for $F_0 = 43.85$; (c), (d) chaotic attractors for $F_0 = 44.75$ and 46.

approximate values of the two incommensurate frequencies for the $F_0 = 43$ dynamo state are 0.0165 and 0.0208 (for the $|\mathbf{B}(0,0,1)|$ time series). For $F_0 = 43.85$, the system becomes periodic or phase locked. The time period of the periodic orbit is relatively large. The emergence of periodic orbit from quasiperiodic solutions is called "phase locking" [32]. A subsequent increase of F_0 leads to a chaotic state, as evident from the phase-space projections for $F_0 = 44.75$ and 46. The nature of attractors is corroborated by the Poincaré sections for $F_0 = 43$, 43.85, 44.75, and 46 presented in Figs. 9(a)–9(d), respectively. These Poincaré sections were obtained by using $|\mathbf{B}(0,0,3)| = 1.15$ as the Poincaré intersection plane for the phase-space trajectories in the subspace of $|\mathbf{B}(0,0,1)|$-$|\mathbf{B}(0,0,2)|$-$|\mathbf{B}(0,0,3)|$. Thus, the chaotic trajectories in the oval A of Fig. 3 appear through the quasiperiodic route via phase locking, first reported for the circle map [32].

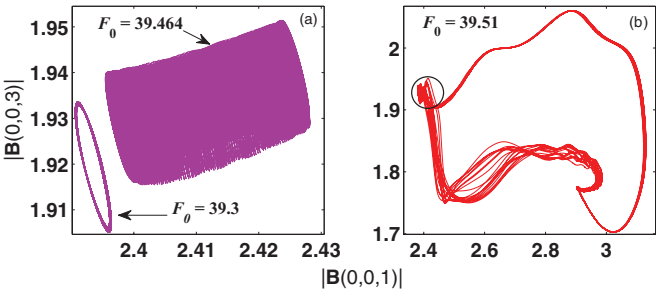

FIG. 10. (Color online) Phase-space projections on the $|\mathbf{B}(0,0,1)|$-$|\mathbf{B}(0,0,3)|$ plane. Panel (a) contains a stable 2-torus ($F_0 = 39.3$) and a 3-torus quasiperiodic state ($F_0 = 39.464$) and panel (b) shows a large chaotic attractor for $F_0 = 39.51$. The corresponding forcing amplitude is marked with an arrow. The circle drawn in (b) portrays a rough phase-space span of the attractors shown in (a).

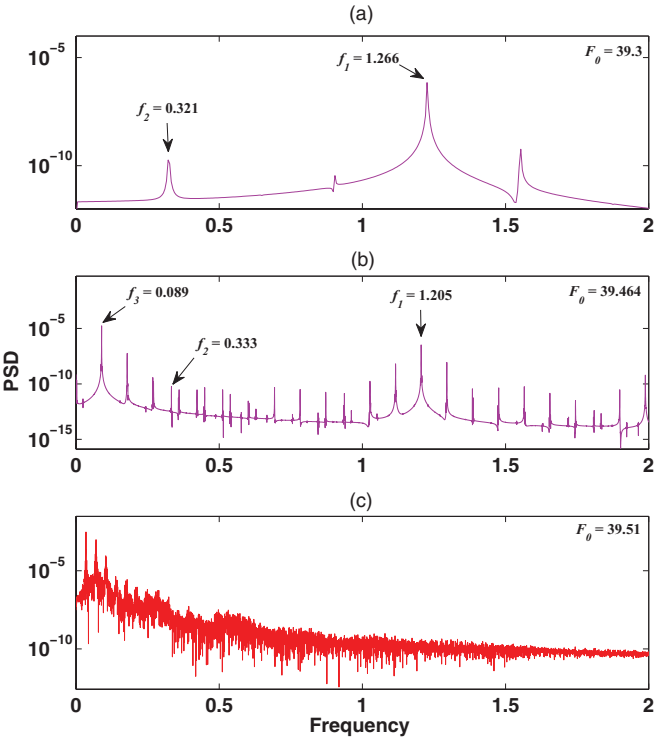

FIG. 11. (Color online) Power spectral density (PSD) plot of the dynamo states shown in Fig. 10 constructed using $|\mathbf{B}(0,0,1)|$ time series. The dominant frequencies are depicted in the figures with arrows. (a) For $F_0 = 39.3$, the state has two incommensurate dominant frequencies. (b) For $F_0 = 39.464$, the state has three incommensurate frequencies. (c) A dense power spectrum corresponding to the large chaotic attractor portrayed in Fig. 10(b).

B. Newhouse-Ruelle-Takens scenario

We observe an interesting set of dynamo states in the rectangular box B of Fig. 3. Figure 10(a) illustrates the phase-space projections on the $|\mathbf{B}(0,0,1)|$-$|\mathbf{B}(0,0,3)|$ plane for $F_0 = 39.3$ and 39.464, corresponding to the two triangular data points in the box B of Fig. 3. Also, the power spectral density plot (PSD) of the $|\mathbf{B}(0,0,1)|$ time series of these two dynamo states is shown in Figs. 11(a) and 11(b). The PSD reveals that the state at $F_0 = 39.3$ contains two incommensurate frequencies f_1 and f_2 [Fig. 11(a)], while the state at $F_0 = 39.464$ has three incommensurate frequencies f_1, f_2, and f_3 [Fig. 11(b)]. Thus, the corresponding dynamo states reside on "2-torus" (T^2) and "3-torus" (T^3), respectively, in the subspace. We expect that a further increase in F_0 should push the system to chaos following a Newhouse-Ruelle-Takens scenario. However, we have not yet found the corresponding chaotic attractor. Recently, Stefani *et al.* [33] have observed similar quasiperiodic routes to chaos in a dynamo model.

Instead of a transition from T^3 to a chaotic dynamo state, a very small increase of F_0 (in the fourth decimal place) pushes the system to a new chaotic attractor, the span of which is much larger than those of the T^2 or T^3. In Fig. 10(b), we illustrate the larger chaotic attractor obtained for $F_0 = 39.51$, corresponding to the square data point in the box B of Fig. 3. In Fig. 10(b), T^2 or T^3 states reside in the circled region. The large attractor for $F_0 = 39.51$ has a different origin, as

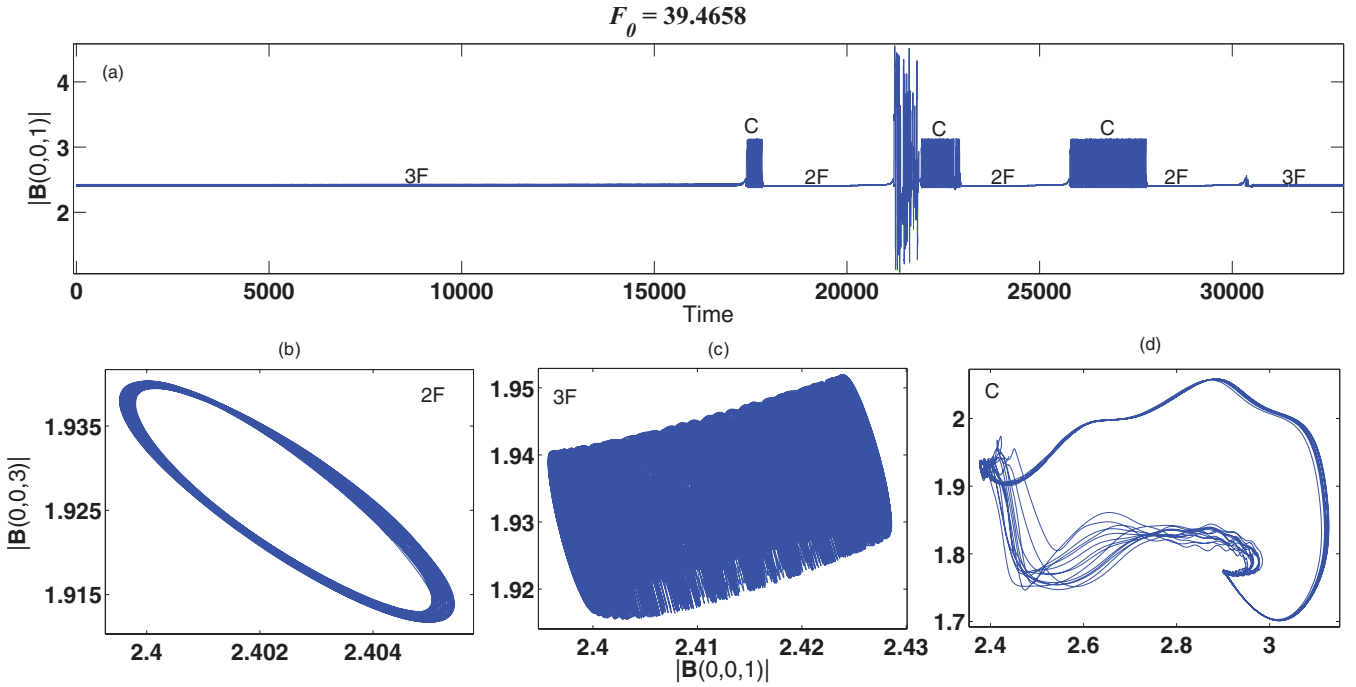

FIG. 12. (Color online) Time evolution of a dynamo state at $F_0 = 39.4658$ showing intermittent transitions among three attractors: quasiperiodic state T^2 (b), quasiperiodic state T^3 (c), and chaotic state (d). Panels (b)–(d) are the phase-space projections at three different time intervals during the evolution.

the PSD shown in Fig. 11(c) is quite different from those in Figs. 11(a) and 11(b). The origin of the larger attractor is not well understood. However, it is possibly through a "crisis." Note that a large number of attractors exist for this range of F_0, as evident from Fig. 3. Chaos can emerge due to merging of multiple attractors or their basins of attraction [32]. A detailed investigation of these issues is beyond the scope of this paper.

We performed dynamo simulations near $F_0 = 39.51$ and observed interesting features involving intermittent transitions between three attractors; this dynamics will be described in the next section.

C. Intermittent transitions between various attractors

For the forcing amplitude $F_0 = 39.4658$, we observe intermittency. A long time series for the $F_0 = 39.4658$ simulation is illustrated in Fig. 12(a), which illustrates that the system makes intermittent transitions among three attractors, 2F, 3F, C, shown below the time series. Note that the 2F, 3F, and C attractors are qualitatively similar to the states shown in Fig. 10, obtained for $F_0 = 39.3$, 39.464, and 39.51, respectively. Thus, at $F_0 = 39.4658$, the system appears to traverse through various attractors. The intermittent transition among various attractors described above is similar to "intermittency" in which a system switches between an "ordered" state and a chaotic state for a single parameter value. In Fig. 12, the quasiperiodic states are the ordered states. The system has been evolved for 50 000 eddy turnover times, and only a part of this time series has been shown in Fig. 12(a). Hence, the observed phenomena are not transient. The large fluctuations near time = 21 250 in Fig. 12(a) are transient fluctuations that settle down quickly.

V. CONCLUSIONS

We performed dynamo simulations with Taylor-Green forcing for Pm = 0.5. We observe bistability with weak- and strong-magnetic-field branches. The dominant magnetic Fourier modes of these branches are $\mathbf{B}(0,0,1)$ and $\mathbf{B}(0,0,2)$, respectively. Both of these branches have subcritical origins. Qualitatively, these branches resemble the weak- and strong-field dynamo actions in rotating magnetoconvection (spherical-shell dynamo) reported earlier [13,16].

Our simulations also reveal various kinds of dynamo states ranging from temporally constant to temporally chaotic ones. We analyzed two chaotic dynamo states in our simulations. Chaos for these parameter windows arise through quasiperiodic routes. One of them undergoes phase locking, while the other appears to go through the Newhouse-Ruelle-Takens route. We also observe intermittent transitions between quasiperiodic attractors (T^2 and T^3) and a chaotic attractor.

Our study and that of Yadav *et al.* [7] on the TG dynamo find dynamo states with time-independent (fixed point), periodic, quasiperiodic, and chaotic magnetic field configurations, which have also been observed in the VKS experiment for different rotation frequencies of the iron propellers [34]. However, there is a major difference between the systems. The TG dynamo for lower Pm appears to show subcritical dynamo transition [4,8], but the VKS experiment exhibits supercritical dynamo transition. Also, the behavior of dynamo transition and dynamo states for Pm = 0.5 discussed in this paper differs significantly from the Pm = 1 TG dynamo studied by Yadav *et al.* [7]. This feature illustrates the richness of the underlying nonlinear MHD equations.

We performed our simulations of the TG dynamo in a periodic box, which is an idealized geometry. Yet, we observe certain similarities between our results and the convective dynamo in rotating spheres, e.g, shift from a supercritical to a subcritical transition with a decrease of magnetic Prandtl number and coexistence of strong- and weak-magnetic-field branches. These similarities could be due to some geometrical resemblance between the two systems as discussed in Sec. III. We need to explore the connection between the TG dynamo and realistic systems such as the spherical-shell dynamo. Also, an extension of this work to lower magnetic Prandtl numbers would yield interesting insights into the challenging problem of MHD dynamo.

ACKNOWLEDGMENTS

We thank B. Sreenivasan, S. Fauve, M. Chandra, and S. Ravichandran for fruitful discussions and comments. We are grateful to one of the anonymous referees for detailed suggestions, especially regarding a possible geometrical connection between the TG dynamo and the convective dynamo with rotation. This work was supported by a research grant of DST India as a Swarnajayanti fellowship to M.K.V. Part of the simulation was done on the VEGA cluster of IIT Madras and the HPC cluster of IIT Kanpur.

[1] H. K. Moffatt, *Magnetic Field Generation in Electrically Conducting Fluids* (Cambridge University Press, Cambridge, 1978).
[2] F. Krause and K. H. Radler, *Mean-field Magnetohydrodynamics and Dynamo Theory* (Pergamon, Oxford, 1980).
[3] A. Brandenburg and K. Subramanian, Phys. Rep. **417**, 1 (2005).
[4] Y. Ponty, J. P. Laval, B. Dubrulle, F. Daviaud, and J. F. Pinton, Phys. Rev. Lett. **99**, 224501 (2007).
[5] G. Nigro and P. Veltri, Astrophys. J. Lett. **740**, L37 (2011).
[6] V. Morin and E. Dormy, Int. J. Mod. Phys. B **23**, 5467 (2009).
[7] R. Yadav, M. Chandra, M. K. Verma, S. Paul, and P. Wahi, Europhys. Lett. **91**, 69001 (2010).
[8] G. Sahoo, D. Mitra, and R. Pandit, Phys. Rev. E **81**, 036317 (2010).
[9] R. Monchaux, M. Berhanu, M. Bourgoin, M. Moulin, P. Odier, J. Pinton, R. Volk, S. Fauve, N. Mordant, F. Pétrélis *et al*., Phys. Rev. Lett. **98**, 044502 (2007).
[10] P. H. Roberts and G. A. Glatzmaier, Rev. Mod. Phys. **72**, 1081 (2000).
[11] M. Ossendrijver, Astron. Astrophys. Rev. **11**, 287 (2003).
[12] F. Pétrélis, N. Mordant, and S. Fauve, Geophys. Astrophys. Fluid Dyn. **101**, 289 (2007).
[13] P. H. Roberts, Geophys. Astrophys. Fluid Dyn. **44**, 3 (1988).
[14] M. G. S. Pierre, in *Solar and Planetary Dynamos*, edited by M. R. E. Proctor, P. C. Matthews, and A. M. Ruchlidge (Cambridge University Press, Cambridge, 1993), pp. 295–302.
[15] S. Stellmach and U. Hansen, Phys. Rev. E **70**, 056312 (2004).
[16] W. Kuang and J. Bloxham, J. Comput. Phys. **153**, 51 (1999).
[17] G. Krstulovic, G. Thorner, J.-P. Vest, S. Fauve, and M. Brachet, Phys. Rev. E **84**, 066318 (2011).
[18] Y. Ponty, P. D. Mininni, D. C. Montgomery, J. F. Pinton, H. Politano, and A. Pouquet, Phys. Rev. Lett. **94**, 164502 (2005).
[19] C. Nore, M. E. Brachet, H. Politano, and A. Pouquet, Phys. Plasmas **4**, 1 (1997).
[20] P. Mininni, Y. Ponty, D. Montgomery, J. Pinton, H. Politano, and A. Pouquet, Astrophys. J. **626**, 853 (2005).
[21] B. Dubrulle, P. Blaineau, O. M. Lopes, F. Daviaud, J. Laval, and R. Dolganov, New J. Phys. **9**, 308 (2007).
[22] E. Dormy and A. M. Soward, *Mathematical Aspects of Natural Dynamos* (CRC Press, Boca Raton, 2007).
[23] N. O. Weiss, Geophys. Astrophys. Fluid Dyn. **105**, 256 (2010).
[24] M. K. Verma, e-print arXiv:1103.2517.
[25] F. Pétrélis and S. Fauve, J. Phys.: Condens. Matter **20**, 494203 (2008).
[26] W. Kuang, W. Jiang, and T. Wang, Geophys. Res. Lett. **35**, L14204 (2008).
[27] P. Pal, P. Wahi, S. Paul, M. K. Verma, K. Kumar, and P. K. Mishra, Europhys. Lett. **87**, 54003 (2009).
[28] A. Kageyama and T. Sato, Phys. Rev. E **55**, 4617 (1997).
[29] S. Childress and A. M. Soward, Phys. Rev. Lett. **29**, 837 (1972).
[30] J. Morin, E. Dormy, M. Schrinner, and J.-F. Donati, MNRAS Lett. **418**, L133 (2011).
[31] B. Sreenivasan and C. A. Jones, J. Fluid Mech. **688**, 5 (2011).
[32] R. C. Hilborn, *Chaos and Nonlinear Dynamics: An Introduction for Scientists and Engineers* (Oxford University Press, Oxford, 1994).
[33] F. Stefani, A. Gailitis, and G. Gerbeth, Astron. Nachr. **332**, 4 (2011).
[34] S. Aumaître, M. Berhanu, M. Bourgoin, A. Chiffaudel, F. Daviaud, B. Dubrulle, S. Fauve, L. Marié, R. Monchaux, N. Mordant *et al*., C. R. Phys. **9**, 689 (2008).